California Institute of Technology

Keck Institute for Space Studies
Postdoctoral Fellowship Final Report

Oliver Gray King

January 2012

Contents

Chapter 1

Introduction

The research I carried out while a Keck Institute Postdoctoral Fellow was focussed on two areas. The first was related to the polarized cosmic microwave background (CMB) – a signal from the dawn of the universe which may contain the clearest view yet of how our universe was born. My research was focussed on two aspects of this: a project to map the polarized emission from our Galaxy, which obscures our view of the polarized CMB, and a project to improve the technology which is being used to directly measure the polarized CMB. These form the subject of Chapters 2 and 3 respectively.

The second theme to my research has been studying relativistic jets in blazars. The relativistic jets which are thought to power blazars are a fascinating astrophysical mystery: in spite of five decades of intensive study we still do not know how relativistic jets are accelerated and collimated, nor what their composition is. We have entered a new era in the study of blazar jets with the launch of the *Fermi* gamma-ray space telescope. It is now possible, for the first time, to monitor the gamma-ray flux of a large number of blazars; this has sparked the advent of very powerful multi-wavelength flux monitoring campaigns from radio through to gamma-ray wavelengths. A particularly important aspect of this multi-wavelength study is that of tying together the variations in flux that are seen across the electromagnetic spectrum. I have focussed on two attempts to improve our understanding of the polarized multi-wavelength emission from blazars, one at optical wavelengths (Chapter 4) and one at radio wavelengths (Chapter 5).

Finally, no research takes place in a vacuum and I owe a debt of gratitude to many for their support. First, I would like to thank the Keck Institute for its generous support. It has been a delight to be associated with it. Thank you to Prof Tony Readhead for your support, mentoring, and access to lab space! Thank you to Rodrigo, Kieran, Tim, Stephen for all your help, and to Russ and Tomi at OVRO for all your hard work.

Chapter 2

The C-Band All-Sky Survey: Characterizing the polarized Galaxy

2.1 Introduction

The C-Band All-Sky Survey (C-BASS) is a 5 GHz survey of the entire sky in total intensity and linear polarization with a resolution of 0.73°. C-BASS aims to provide accurate maps of the polarization of Galactic synchrotron radiation with high signal-to-noise ratio and uncorrupted by Faraday rotation. The survey is being conducted in two parts. For the Northern sky, a new 5 GHz instrument has been deployed on a 6.1-m parabolic antenna at the Owens Valley Radio Observatory (OVRO), California – shown in Figure 2.1. For the Southern sky a similar instrument is used on a 7.6-m telescope at the MeerKAT support site near Carnarvon, South Africa.

C-BASS maps will be of great value in studies of the polarization of the cosmic microwave background radiation (CMB). CMB polarization is being measured by the *WMAP* (Larson et al., 2011) and *Planck* satellites, and by several current and future ground-based and balloon-borne experiments, e.g. QUIET Collaboration et al. (2011); Chiang et al. (2010). A major goal for these experiments is to measure the *B*-mode polarization signal, which is expected to provide information about the epoch of inflation – in particular, the energy scale of inflation – and about physics at grand unification energies. In order to do this the CMB must be separated from foreground emission with higher accuracy than is possible with our current understanding of Galactic foregrounds. C-BASS data will significantly improve the accuracy of foreground subtraction. In addition to being useful for polarized foreground subtraction from CMB measurements, C-BASS will provide a wealth of data on the nature of the Galactic magnetic field, help firm constraints on so-called "anomalous" emission in conjunction with other large-area surveys, and provide more data on the Galactic cosmic ray electron population. C-BASS will allow an accurate separation of synchrotron, free-free, and anomalous emission.

The Northern C-BASS receiver is designed to measure both total intensity and linear polarization with minimal systematic error. To achieve this we developed a novel hybrid receiver design: the total intensity is measured in a continuous-comparison fashion by comparing the sky temperature against a cold electrical reference load, the linear polarization is measured by correlating orthogonal circular polarization signals from the horn. These receiver architectures suppress the instabilities inherent in radiometers and those induced by environmental changes.

Figure 2.1: The C-BASS telescope at the Owens Valley Radio Observatory.

I have been involved in the C-BASS project since its inception. My DPhil work involved designing and building the Northern receiver; as part of my Keck Institute Fellowship work I have developed a sophisticated mathematical model of the receiver, developed an instrument calibration procedure, and contributed to the data reduction pipeline. In this section I describe the receiver modeling, based largely on the upcoming paper King et al. (2012).

2.2 C-BASS Instrument Design

The Northern C-BASS receiver is a novel hybrid of a continuous comparison radiometer and a correlation polarimeter, covering the 4.5 to 5.5 GHz band in a single analog channel. A schematic representation of the receiver is shown in Figure 2.2. This receiver architecture was chosen to provide stable measurements of both total intensity (Stokes I) and linear polarization (Stokes Q and U). The detector diode voltages are digitized and processed in a custom-designed digital backend.

Total intensity is measured by pseudo-correlating both orthogonal circular polarizations against independent reference loads. This style of radiometer, called a continuous comparison radiometer, is similar to that used in both the *WMAP* (Jarosik et al., 2003) and *Planck* (Davis et al., 2009) receivers, though both the *WMAP* and *Planck* receivers operated on linear rather than circular polarizations. Like the *Planck* receivers, we compare orthogonal polarization signals against electrical refence loads, rather than signals from a second sky horn, i.e. like the *WMAP* receivers. This preserves the optical purity of the receiver by having an on-axis optical system. The electrical reference loads are temperature controlled RF terminations. Suppression of receiver gain drifts, given unequal sky and reference load temperatures, can be improved through the use of an r-factor correction (Mennella et al., 2003).
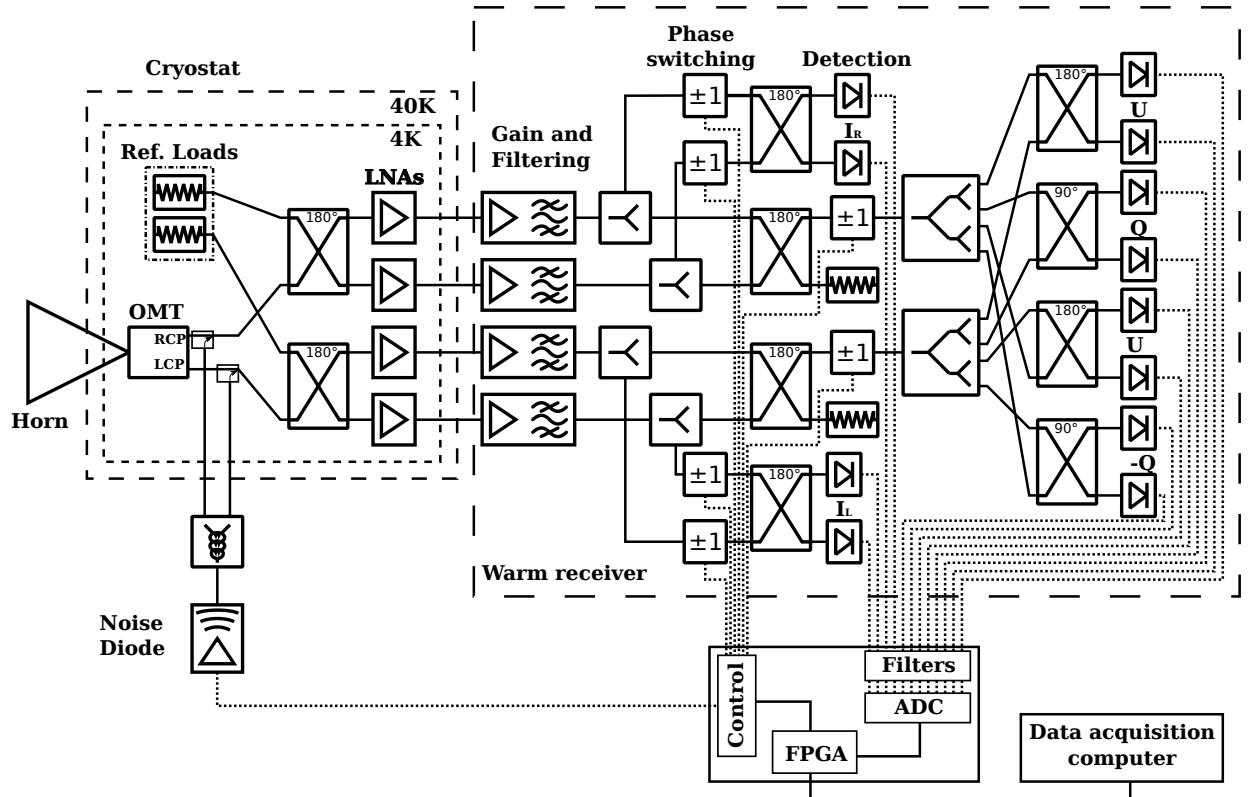
Figure 2.2: A simplified schematic diagram of the C-BASS receiver. Left and right circular polarizations are extracted from the feed horn and combined with temperature-controlled reference loads using 180° hybrids. After gain and filtering a bank of 180° hybrids pseudo-correlates the total intensity signals and recovers the circular polarization voltages, which are fed into the correlation polarimeter section. The detected powers are digitized and processed by an FPGA-based digital readout system and then stored on disk.

We expect that the diffuse Galactic synchrotron emission will have a negligible circularly polarized component. In this case, each orthogonal circular polarization measured by the receiver will be a noise-independent measure of the sky signal total intensity. The continuous comparison radiometer provides a more stable measurement of total intensity, at the expense of increased receiver noise over a simple radiometer.

The receiver measures both Stokes Q and U simultaneously in a correlation fashion. When E_l and E_r, the left-circular and right-circular polarization voltages respectively, are pseudo-correlated using a 180° hybrid we obtain Stokes U. When they are pseudo-correlated with a 90° hybrid we obtain Stokes Q. In the C-BASS receiver E_l and E_r are pseudo-correlated in all possible combinations to provide two measures of each linear polarization parameter and maintain receiver symmetry.

2.3   Receiver Modelling

Realistic receiver modelling allows us to develop accurate data calibration procedures, and guides the receiver design process by identifying the most important component parameters. We would like to be able to describe each component in a receiver using a realistic model which includes noise and non-ideal component performance. The model should then produce descriptions of the receiver outputs which include the

imperfections and noisy behavior of the network of receiver components. It is useful if this can be done analytically.

Most previous analytic and semi-analytic approaches to characterizing systematic effects in receivers have employed Jones matrices to describe receiver components and Mueller matrices to characterize the effects of receiver systematics on the observed Stokes parameters, e.g. Carretti et al. (2001); Hu et al. (2003); O'Dea et al. (2007). In this formulation the propagation of radiation through a receiver can be described by a 2x2 Jones matrix $\mathbf{J}$, such that the electric field after passing through the receiver is

$$\mathbf{E}_{\text{out}}(t) = \mathbf{J}\mathbf{E}_{\text{in}}(t)$$

where $\mathbf{E}_{\text{in}}(t)$ is the incident electric field vector, and $\mathbf{E}_{\text{out}}(t)$ is the output signal. The response of a cascaded series of components in an instrument can then be found by multiplying their Jones matrices. The Mueller matrix which corresponds to Jones matrix $\mathbf{J}$ is given by $\mathbf{T}(\mathbf{J} \otimes \mathbf{J}^*)\mathbf{T}^{-1}$ (Hamaker et al., 1996).

2.3.1 Scattering Matrix Modelling

The scattering matrix approach is capable of modelling noise along with the signal propagation. In the scattering matrix formulation any arbitrary component or network of components (excluding detectors) can be described by a frequency-dependent scattering matrix $\mathbf{S}(\nu)$. I omit the frequency dependence from now on for the sake of brevity.

The scattering matrix relates the incident, reflected, and transmitted waves that travel on transmission lines attached to the N ports of a linear network. It provides a complete description of an N-port network as seen at its N ports (Pozar, 2005). This formulation can be extended to optical systems and used to describe instruments which contain both optical components, such as lenses or mirrors, and microwave circuit techniques, such as horns, transmission lines, filters, etc. (Zmuidzinas, 2003).

Scattering and noise matrices

Consider an arbitrary N-port network. We denote the incident wave at port i by V_i^+, the reflected wave by V_i^-, and the noise wave produced by the network at that port by c_i. These quantities are related by the scattering matrix $\mathbf{S}$ and noise wave vector $\mathbf{c}$ as:

$$\begin{bmatrix} V_1^- \\ V_2^- \\ \vdots \\ V_N^- \end{bmatrix} = \begin{bmatrix} S_{11} & S_{12} & \cdots & S_{1N} \\ S_{21} & & & \vdots \\ \vdots & & & \\ S_{N1} & \cdots & & S_{NN} \end{bmatrix} \begin{bmatrix} V_1^+ \\ V_2^+ \\ \vdots \\ V_N^+ \end{bmatrix} + \begin{bmatrix} c_1 \\ c_2 \\ \vdots \\ c_N \end{bmatrix} \tag{2.1}$$

The scattering matrix $\mathbf{S}$ is unitary if the device is lossless and reciprocal networks have symmetric scattering matrices (Pozar, 2005).

The noise wave voltages c_i of an N-port network are complex time-varying random variables characterized

by a correlation matrix $\mathbf{C}$

$$
\begin{aligned}
\mathbf{C} &= \langle \mathbf{c} \otimes \mathbf{c}^{\dagger} \rangle \\
&=
\begin{bmatrix}
\langle |c_1|^2 \rangle & \langle c_1 c_2^* \rangle & \cdots & \langle c_1 c_N^* \rangle \\
\langle c_2 c_1^* \rangle & & & \vdots \\
\vdots & & & \\
\langle c_N c_1^* \rangle & \cdots & & \langle |c_N|^2 \rangle
\end{bmatrix}
\end{aligned}
\tag{2.2}
$$

where the angle brackets indicate time averaging, $\dagger$ indicates the conjugate transpose operation, and $\otimes$ indicates the outer product (or Kronecker product). The diagonal terms of $\mathbf{C}$ give the noise power deliverable at each port in a 1 Hz bandwidth. The off-diagonal terms are correlation products. The noise correlation matrix $\mathbf{C}$ for a passive network is determined from its scattering matrix $\mathbf{S}$ by (Wedge & Rutledge, 1991)

$$
\mathbf{C} = kT(\mathbf{I} - \mathbf{S}\mathbf{S}^{\dagger})
\tag{2.3}
$$

where k is Boltzmann's constant, T is the physical temperature of the network, and $\mathbf{I}$ is the identity matrix. The noise correlation matrix for an active network can be determined by measurement or modelling.

Solving the network response

We build a network of N-port devices, connected by nodes, and assign scattering matrices and noise correlation matrices to each device. Once all the components in a receiver have been described by scattering and noise correlation matrices, the task remains to calculate the scattering matrix and the noise wave vector which describe the receiver as seen at its inputs and outputs. I developed a `MATLAB` package called `SNS`[1] (King, 2010) to do this. It implements algorithms which solve for the network response and can operate on both analytic and numeric descriptions of scattering and noise correlation matrices. It is capable of solving for the signal and noise behavior of arbitrarily connected networks of components.

2.4 C-BASS Receiver Model and Systematic Errors

The receiver schematic shown in Figure 2.2 accurately represents the action of the receiver, though it is not a facsimile of the actual receiver diagram. Long gain chains, composed of multiple amplifiers, attenuators, filters, isolators, and slope compensators are represented by a single amplifier. Not all components are modeled as producing noise, though all significant sources are modeled. A fully-parameterized component-for-component reproduction of the real receiver is not suitable for analytic description; the elements of the Mueller matrix become so complex as to be meaningless and would fail to illuminate the important lessons that can be learnt using a simpler, but representative, model.

2.4.1 Receiver Data Channels

In King et al. (2012) I show how it is possible to rewrite the power detected at each receiver output in terms of contributions from the sky (written in terms of Stokes parameters) and contributions from noisy components in the receiver. This allows us to create a description of each receiver data channel in a framework which is

---

[1]Download at http://www.astro.caltech.edu/~ogk/SNS/

powerful and natural to radio astronomy. We will be able to express the vector $\mathbf{r}$ of receiver data channels (power per unit bandwidth) in the form:

$$\mathbf{r} = \begin{bmatrix} r_I \\ r_Q \\ r_U \\ r_V \end{bmatrix} = k_B \Big(\mathbf{M}_{\mathrm{corr}} \big(\mathbf{M}_{\mathrm{OMT}} \mathbf{e}^S + \mathbf{N}_{\mathrm{OMT}} \big) + \mathbf{N}_{\mathrm{corr}} \Big)$$

$$= k_B \Big(\mathbf{M}_{\mathrm{rec}} \mathbf{e}^S + \mathbf{N}_{\mathrm{rec}} \Big)$$

$$\text{where}:$$

$$\mathbf{M}_{\mathrm{rec}} = \mathbf{M}_{\mathrm{corr}} \mathbf{M}_{\mathrm{OMT}}$$

$$\mathbf{N}_{\mathrm{rec}} = \mathbf{M}_{\mathrm{corr}} \mathbf{N}_{\mathrm{OMT}} + \mathbf{N}_{\mathrm{corr}} \tag{2.4}$$

Here we have split the receiver into two parts at the point where the noise diode calibration signal is injected. We refer to the pre-calibration signal injection part of the receiver as the OMT section, and the post-signal injection part as the correlator section. $\mathbf{M}_{\mathrm{OMT}}$ and $\mathbf{M}_{\mathrm{corr}}$ are the Mueller matrices for the OMT and correlator sections respectively, and $\mathbf{N}_{\mathrm{OMT}}$ and $\mathbf{N}_{\mathrm{corr}}$ are the contributions of noise sources in the OMT section and correlator section (amplifiers, lossy components, calibration noise sources) respectively to an offset in each data stream. The action of the telescope optics (reflectors and horn) can be included by prepending its Mueller matrix to the Mueller matrix chain.

The Mueller matrices, offset terms, and Stokes parameters in Equation 2.4 are frequency dependent – $\mathbf{r}$ is a vector with units of power per unit bandwidth. Any matrix multiplication has to be done for each frequency separately, and the power integrated over the band at the end. This requires a source spectrum for the Stokes parameters.

2.4.2 Analysis Procedure

I constructed a receiver model using `SNS` and the `MATLAB` symbolic algebra toolbox in which all the components have fully parameterized scattering matrices as described in §2.4.3. I perform the computationally-expensive steps of calculating the receiver scattering matrix and noise wave vector, and deriving the Mueller matrix $\mathbf{M}_{\mathrm{rec}}$ and noise vector $\mathbf{N}_{\mathrm{rec}}$, only once.

2.4.3 Component Models

In general there are three levels of non-ideality in receiver components: those implicit in the design, random variations from device to device, and measurement errors. For the components in the C-BASS receiver the non-ideal behavior implicit in the design was generally dominant: device to device variations were substantially lower and measurement error was negligible. In King et al. (2012) we develop detailed, fully parameterized models for all the components in the C-BASS receiver and used them to calculate an accurate model of the receiver output.

2.4.4 Full Receiver Model

The full error model for the correlation receiver is given by:

$$\mathbf{M}_{\mathrm{corr}} = \begin{bmatrix} \alpha_I G_\Sigma & 0 & 0 & \alpha_I G_\Delta \\ 0 & \alpha_Q G_{Pc} & \alpha_Q G_{Ps} & 0 \\ 0 & -\alpha_U G_{Ps} & \alpha_U G_{Pc} & 0 \\ \alpha_I G_\Delta & 0 & 0 & \alpha_I G_\Sigma \end{bmatrix} \tag{2.5}$$

This Mueller matrix shows the advantage of using a correlation architecture – in spite of using imperfect components, we have no leakage of total intensity into our polarization channels! The parameters G_{Pc}, G_{Ps} are a cosine/sine pair for small phase error amplitude and hence form a rotation matrix which describes the action of the receiver on the polarization vector.

The vector of noise contributions to the data channels is:

$$\mathbf{N}_{\mathrm{corr}} =$$
$$\begin{bmatrix} -\alpha_I \Big\{ G_L T_A + G_R T_B - G_\Sigma D\Big(L T_{ND} + (1-L) T_{\mathrm{amb}} \Big) \Big\} \\ \alpha_Q G_{Ps} D[L T_{ND} + (1-L) T_{\mathrm{amb}}] \\ \alpha_U G_{Pc} D[L T_{ND} + (1-L) T_{\mathrm{amb}}] \\ -\alpha_I \Big\{ G_L T_A - G_R T_B - G_\Delta D\Big(L T_{ND} + (1-L) T_{\mathrm{amb}} \Big) \Big\} \end{bmatrix} \tag{2.6}$$

The noise vector is not a measure of the variance of the measured signal: it is the systematic offset in each data channel due to noise produced in the instrument. Offsets due the noise produced by the amplifier chains is perfectly cancelled by the demodulation and diode differencing steps.

2.4.5 Calibrating the receiver

The primary function of the noise diode is to calibrate the receiver. The calibration has two goals:

1. Scale all data channels to the same temperature scale. The total intensity and polarization channels have different gains and a calibration signal of known intensity and polarization properties can be used to scale them appropriately.

2. Measure the polarization rotation introduced by the post-coupler electronics. This is likely to be temperature, and hence time, dependent.

If we turn the noise diode on and off in rapid succession and measure the difference in the receiver channels we get:

$$\Delta \mathbf{r} = \begin{bmatrix} \alpha_I G_\Sigma D L \Delta T_{ND} \\ \alpha_Q G_{Ps} D L \Delta T_{ND} \\ \alpha_U G_{Pc} D L \Delta T_{ND} \\ \alpha_I G_\Delta D L \Delta T_{ND} \end{bmatrix} \tag{2.7}$$

We can use $\Delta \mathbf{r}$ to correct for some of the errors seen in $\mathbf{M}_{\mathrm{corr}}$ and both scale the outputs and correct for the instrumental polarization rotation.

Instrument calibration

Using this model of the C-BASS receiver I then derived a calibration routine, and wrote the instrument calibration parts of the C-BASS data reduction pipeline. The receiver calibration routine takes place in two steps. First, the noise diode is used to perform an instrument calibration step. Second, the noise diode scale is calibrated against astronomical sources to determine its flux density, which is transferred to the Stokes data.

The C-BASS receiver produces two measurements of total intensity – one of each circular polarization – and a measurement of the linear polarization vector. We can rewrite the data channels as:

$$\mathbf{r} = \mathbf{E}\left(\mathbf{M}_{\mathrm{corr}}\left\{\mathbf{M}_{\mathrm{OMT}}\mathbf{S}_T + \mathbf{N}_{\mathrm{OMT}} + \mathbf{A}(\lambda, \mu) + \mathbf{T}_d(t)\right\} - \mathbf{N}_{\mathrm{ref}}\right) \tag{2.8}$$

Here $\mathbf{S}_T$ is the true Stokes vector present at the input, $\mathbf{N}_{\mathrm{OMT}}$ is vector of offsets in each data channel coming principally from the OMT (it includes offsets due to amplifier input noise leaking from one channel to another), and $\mathbf{A}(\lambda, \mu)$ is a vector of ground spillover. The other quantities are:

$$\mathbf{E} = \begin{bmatrix} \alpha_I & 0 & 0 \\ 0 & \alpha_Q & 0 \\ 0 & 0 & \alpha_U \end{bmatrix}, \mathbf{M}_{\mathrm{corr}} = \begin{bmatrix} G_\Sigma & \mathbf{0} \\ \mathbf{0} & G_p \mathbf{R}(-\phi) \end{bmatrix}, \mathbf{M}_{\mathrm{OMT}} = \begin{bmatrix} \Lambda_I & \mathbf{g} \\ \mathbf{f} & \Lambda_P \mathbf{R}(-2(\theta_0 + \phi_p)) \end{bmatrix}$$

$$\mathbf{T}_d(t) = \begin{bmatrix} 1 \\ 0 \\ 1 \end{bmatrix} T_d(t), \mathbf{N}_{\mathrm{ref}} = \begin{bmatrix} G_L T_A + G_R T_B \\ 0 \\ 0 \end{bmatrix} \tag{2.9}$$

The parameters in these matrices are identified by observing sources of known flux density and polarization, primarily the supernova remnant Taurus A, and through the use of sky dips. Furthermore, residual 1/f noise in the data channels are removed by the mapping component of the pipeline, based on the DESCARTES mapping routines.

2.5   C-BASS Maps

I show several maps produced by the Northern C-BASS instrument over the last few months in Figure 2.3. The Northern-sky map is displayed in Galactic coordinates with an arbitrary color scale. The Galactic plane, along with several well-known Galactic features such as supernova remnants and star-forming regions are clearly. I also show close-up maps of the polarized point source Tau A and the unpolarized star-forming region DR21. These show that the polarization channel is working correctly, with very low leakage of total intensity into the polarization channel.
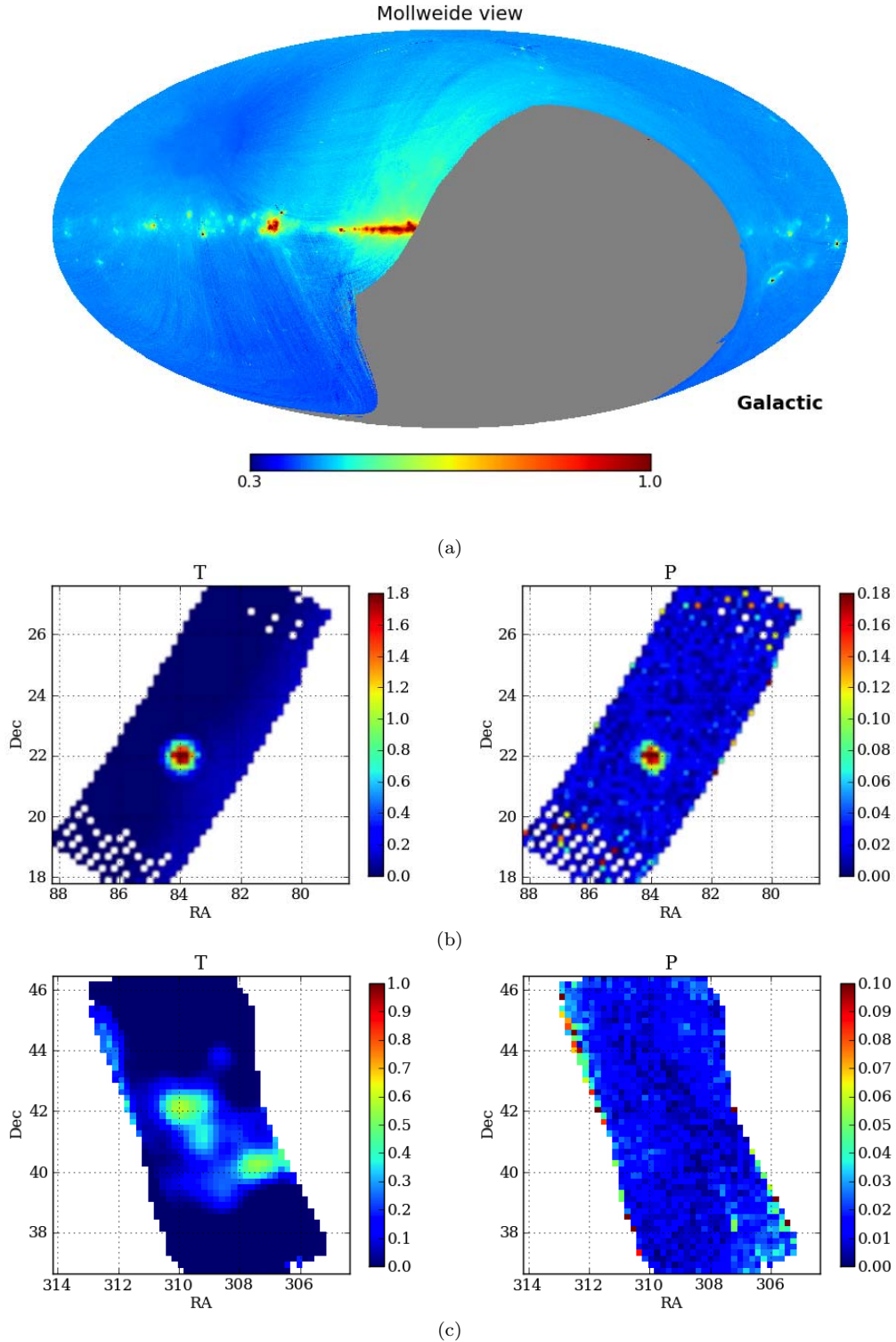
Figure 2.3: All maps courtesy of the C-BASS collaboration. (a) Map of the total intensity sky based on several weeks of data, in Galactic coordinates and with an arbitrary temperature scale. Several supernova remnants (arcs) as well as several well-known Galactic structures are clearly seen. (b) Map of the polarized supernova remnant Tau A. The polarization signal ($\sim 8\%$ amplitude) can clearly be seen. (c) Map of the unpolarized Galactic star forming region DR21. No polarization signal is seen, indicating that leakage of total intensity into the polarization channel is very small, $< 1\%$.

Chapter 3

QUIET Module Modeling

3.1 Introduction

Techniques for the measurement of the polarization of an electromagnetic wave can be divided into two categories: measurement by differencing and measurement by correlation. The approaches differ markedly in their technical implementation and suffer from different sources of systematic error in their measurements. The question of which approach to take in measuring linear polarization is largely determined by which class of technology is more sensitive at the wavelength of interest.

At frequencies of tens of GHz to ~ 100 GHz two technology types are competitive in terms of sensitivity: coherent detectors based on low-noise transistors and incoherent detectors based, typically, on bolometers. Coherent detectors respond to the complex amplitude of the field – both amplitude and phase – while incoherent detection instruments respond to the intensity – photon counters. Correlation polarimeters are usually implemented using a coherent approach; they contain low-noise amplifiers (LNAs) and may also be heterodyne (contain a frequency mixer). Differencing polarimeter architectures are typically used with incoherent detectors, such as hot-electron bolometers (HEBs), microwave kinetic inductance detectors (MKIDs), or transition-edge sensor bolometers (TES).

The sensitivity of coherent detectors is fundamentally limited by quantum noise because they contain phase-preserving amplifiers (Caves, 1982). The quantum limit on the noise temperature of an amplifier is given by $T_{QL} = h\nu/k \simeq \nu[\text{GHz}]/20$. Incoherent-detector based polarimeters are fundamentally more sensitive as they are not limited by quantum noise. Whether this fundamental sensitivity can be achieved is a more complicated question, with practical considerations like receiver cooling, band-defining filters, and detector size becoming important. Incoherent polarimeters are background-limited by the photons produce by the detector itself, the telescope it is housed in, and the atmosphere – some of which can be reduced by placing the detector in space. Below 56 GHz the irreducible background that is the cosmic microwave radiation hands the sensitivity advantage to coherent detectors. This renders the quantum limit irrelevant to the sensitivity argument at radio frequencies (Zmuidzinas, 1999).

Correlation polarimeters do not need cooled correlators – amplification of the electric field has rendered the correlator noise negligible. This is an advantage over incoherent detectors, in which the entire receiver (up to and including the power detection stage) needs to be cooled. Occupation of the focal plane in multi-pixel receivers is another consideration: correlation polarimeters can measure both Q and U simultaneously in a single feed (pixel), while differencing polarimeters require two feeds, or a feed rotation, to perform the
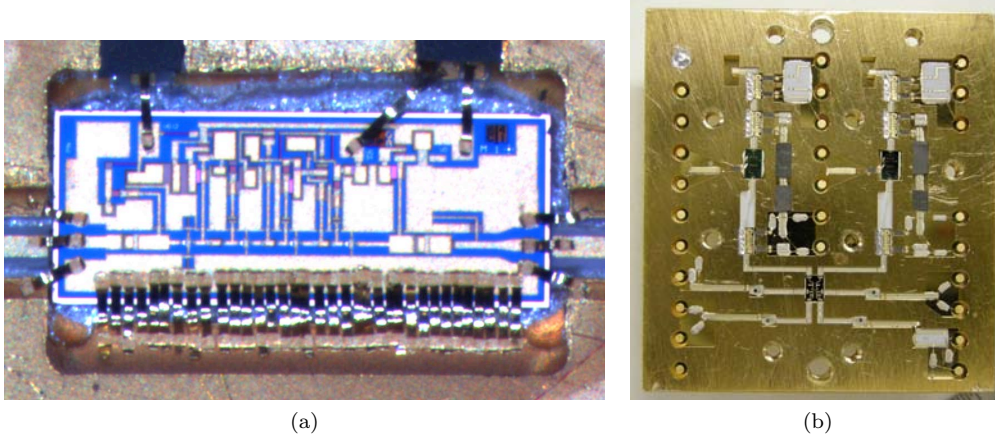
<div align="center">(a)   (b)</div>

Figure 3.1: (a) A MMIC low noise amplifier in a QUIET receiver. The MMIC chip is $\sim 2 \times 0.7$ mm in size and has all the biasing circuitry integrated on the substrate. (b) The interior of a QUIET receiver block. Signals from the sky enter in waveguide at the top, are amplified by several stages of MMIC LNAs, and are phase-discriminated and detected at the bottom. The low-frequency signals corresponding to sky polarization exit the block and are digitized. The block is approximately 1" square. Pictures courtesy K. Cleary.

same measurement. This is because in coherent detectors the signal can be copied without adding significant noise, as long as this copying (signal splitting) happens after the electric field has been amplified.

The sum of all these considerations means that, in practice, at cm-wavelengths and longer correlation polarimeters are the technology of choice. The frequency spectrum around 100 GHz is disputed territory, with both coherent and incoherent polarimeters being used in CMB polarization experiments. At frequencies of hundreds of GHz incoherent differencing polarimeters currently have an undisputed sensitivity advantage.

3.2 QUIET

3.2.1 Scientific Goal

The QUIET experiment (Cleary, 2010; Collaboration et al., 2011) operated receivers at 43 GHz (Q-band) and 90 GHz (W-band) on a telescope in the Atacama Desert in Chile. It aimed to measure polarized radiation from the cosmic microwave background (CMB). The spatial pattern of the polarized CMB is determined by, among other things, gravitational waves during the first $\sim 10^{-32}$ seconds after the Big Bang (the so-called "inflationary epoch"). The detection of the inflationary signature in the CMB is a major goal of modern cosmology. It is, however, an extremely faint signature requiring the most sensitive detectors and years of observing to detect. To date, it has not been detected though a swathe of experiments have placed constraints on its strength.

3.2.2 Technology

The QUIET detectors are based on MMIC (Monolothic Microwave Integrated Circuit) technology. In this technology, the transistor-based amplification circuits are integrated onto a single substrate. This allows a higher level of integration than is possible with traditional discrete circuits, and results in significantly more compact receivers. This reduction in the space needed to house a single feed makes it feasible to place an

array of feeds in the focal plane of a telescope. An example of a MMIC chip and a QUIET detector block are shown in Figure 3.1.

3.3 Modeling

Several improvements in W-band MMICs are needed before it will be feasible to detect the gravitational wave signature in the polarized CMB with instruments based on them. Most crucial is the noise produced by the MMIC LNAs. These MMICs need to be embedded in a block without significant degradation in their performance.

I undertook a modeling program as part of the technology R&D for the next generation of MMIC-based W-band polarimeters. The purpose of this program was to determine, via sophisticated 3D electromagnetic modeling, whether any degradation in the sensitivity of the MMIC devices would result from their being placed in a block.

3.3.1 3D EM Modeling

The sensitivity of a coherent receiver is largely determined by the first LNA in the signal processing chain. I began by building a model of the first cavity of the QUIET block in the 3D EM simulation software package HFSS[1]. This model is shown in Figure 3.2.

This model allowed me to test a number of questions about the module design which in the past would have required expensive prototypes to be machined, assembled and tested. These simulations will inform the design of the next generation of W-band receiver arrays. A sample of these questions, and their answers, are listed here:

- Does the 90 deg bend in the waveguide probe adversely affect the impedance match to the input of the LNA? **No**.

- Is the performance highly sensitive to whether the LNA MMIC is fed by a microstrip line or a CPW line from the waveguide probe? **No**.

- Is it necessary to connect the top ground plane of the LNA MMIC to the cavity ground? **Yes**. If yes: do ribbon bonds – which may be used in the automated assembly of a large number of modules – provide the same effect as indium foil, which it is necessary to place by hand? **Yes, below 105 GHz**. See Figure 3.3 for models and simulated results.
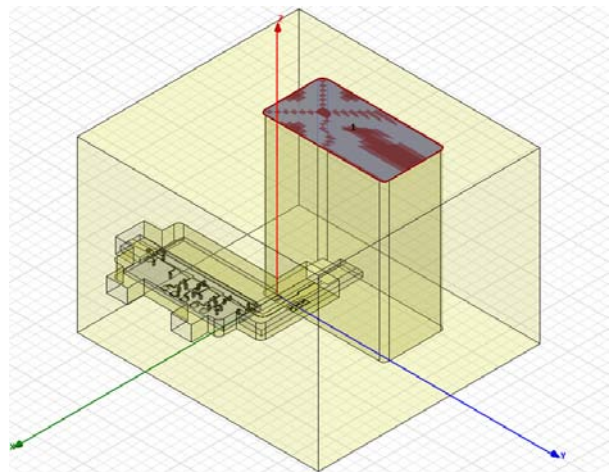

Figure 3.2: Full 3D model of the first cavity of the QUIET module with embedded MMIC amplifier, built in HFSS. The waveguide input port is shaded red and grey. A waveguide probe feeds a MMIC LNA. The output of the MMIC LNA exits the cavity via a microstrip transmission line to feed the second-stage LNA (not shown).

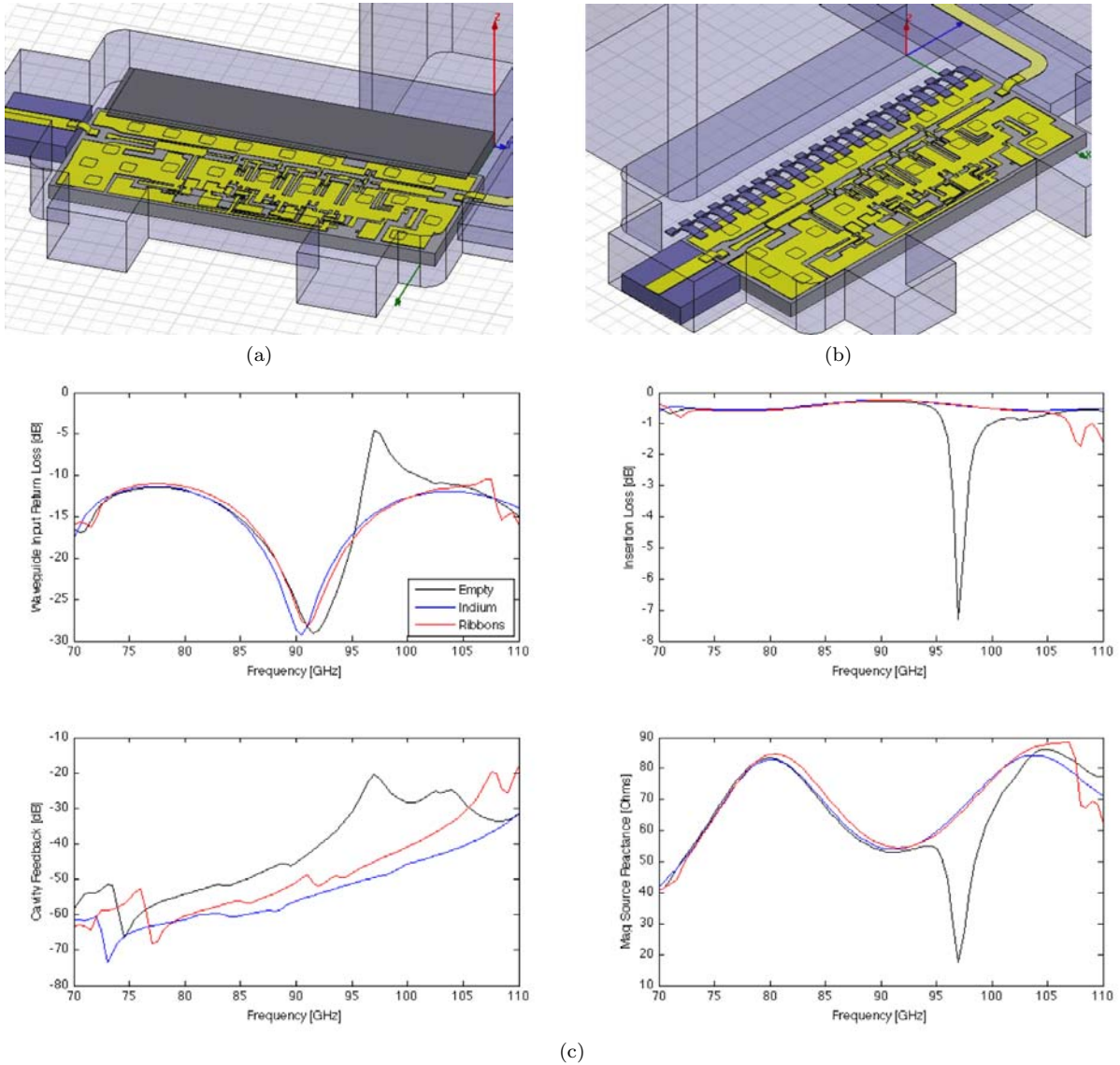
[1] www.ansoft.com/products/hf/hfss/

(a)

(b)

(c)

Figure 3.3: (a) Model of the MMIC cavity for the first LNA in the QUIET module, with grounding of the top-side ground plane provided by indium foil (grey slab). (b) The case where grounding is provided by ribbon bonds. (c) Simulated performance of the indium and ribbon cases, as well as the case where no top-side grounding is provided ("empty"). There is little difference between the indium foil and ribbon bond cases below 105 GHz. The case where there is no top-side grounding has significantly worse cavity feedback, return loss, and transmission.
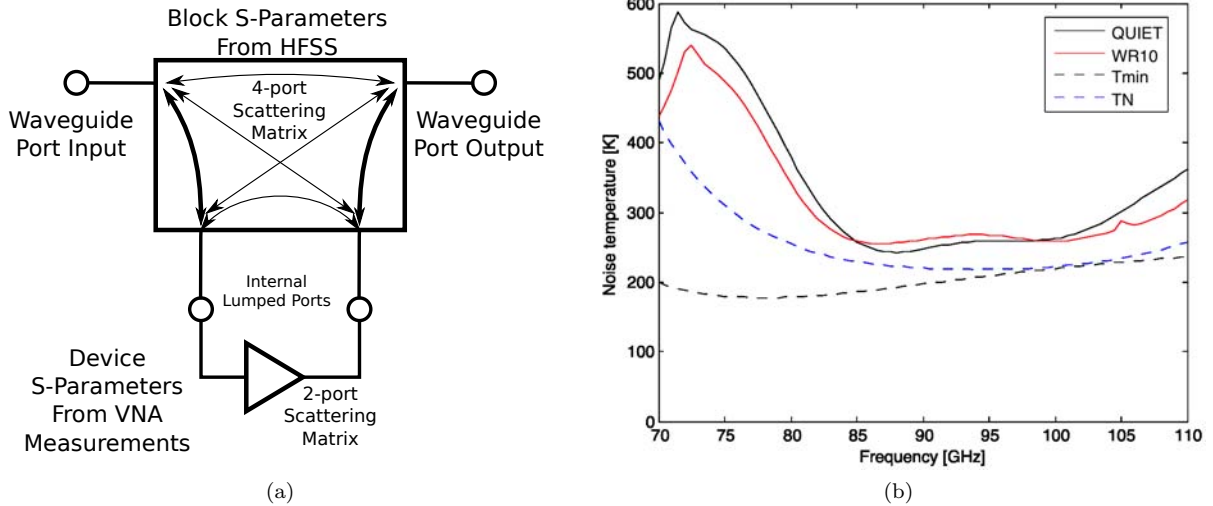
14

Figure 3.4: (a) How to combine the passive 3D EM simulation results from HFSS with measured or simulated MMIC LNA performance. (b) The simulated noise temperature of a room-temperature LNA MMIC placed in two different types of cavities, a QUIET module and a JPL WR10 block. The fundamental noise performance of the MMIC LNA when matched to a 50Ω input is indicated by the blue dashed line (T_N), and the minimum possible noise temperature (assuming perfect input noise matching) is shown by the black dashed line (T_{min}). There is little difference between the QUIET module performance and the WR10 block, though the performance of both blocks may be improved by changing the impedance of the waveguide probe which feeds the LNA.

3.3.2 Full Noise Modeling

Of critical importance to MMIC-based receivers is whether the performance of a MMIC device is degraded when it is housed in a block. Crucially, is the receiver noise temperature the same as the noise temperature of the first LNA? To determine this it is necessary to combine 3D simulations of the response of the block (see previous subsection) with complex signal and noise models of the MMIC LNA in question.

I calculated this by combining HFSS simulations of the block performance with ADS and Microwave Office simulations of the LNA performance. This was done using a MATLAB library I wrote called SNS (King, 2010), which allows one to solve for the full noise and signal performance of an arbitrarily connected network of components.

The schematic representation of the network created in SNS is shown in Figure 3.4a. A 4-port scattering matrix obtained from the HFSS simulation is combined with a 2-port scattering matrix and noise correlation matrix which describe the performance of the LNA.

This simulation was performed with two different block designs: the QUIET cavity model in Figure 3.2 and the JPL WR10 block (not shown). The noise temperature simulation is shown in Figure 3.4b. There was little difference between the room-temperature performance of the QUIET block and the WR10 block, though both could be improved by better impedance matching on the waveguide probe which feeds the LNA.

15

Chapter 4

RoboPol: Monitoring the optical linear polarization of blazars

4.1 Introduction

The relativistic jets which are thought to power blazars are a fascinating astrophysical mystery: in spite of five decades of intensive study we still do not know how relativistic jets are accelerated and collimated, nor what their composition is. We have entered a new era in the study of blazar jets with the launch of the *Fermi* gamma-ray space telescope. It is now possible, for the first time, to monitor the gamma-ray flux of a large number of blazars; this has sparked the advent of very powerful multi-wavelength flux monitoring campaigns from radio through to gamma-ray wavelengths. A particularly important aspect of this multi-wavelength study is that of tying together the variations in flux that are seen across the electromagnetic spectrum: optical polarization, which probes the strength and structure of the magnetic field in the relativistic jet, provides the key to this.

I have helped to start, and am now the project manager of, the RoboPol project. RoboPol will be the most powerful optical polarization monitoring program to date. Our data, combined with realistic simulations with full 3-D relativistic MHD code, *Fermi* gamma-ray data, and multi-wavelength flux monitoring data, will have the potential to finally untangle the mysteries of blazar jets.

4.2 Physics of Blazars

Blazars are the most active galaxies. The blazar phenomenon is believed to be the observable end-result of the non-thermal radiation from a relativistic jet, which is powered by an accreting supermassive black hole and directed at a small angle with respect to our line of sight Blandford & Konigl (1979). For this reason, blazars are an ideal laboratory to study the cosmic growth of black holes, the physics of accretion and the launching of relativistic jets, the formation and propagation of disturbances and shocks along these jets, and the acceleration of non-thermal particle populations to very-high energies (at least 10^8–10^{14} eV, and possibly up to 10^{21} eV).

The jet outflows themselves are created relativistically and often maintain relativistic propagation speeds (with bulk Lorentz factors $\Gamma \sim 10$) out to large radii. Jets can be imaged in radio waves using Very Long Baseline Interferometry (VLBI), on radial scales from 10^{10} m to $> 10^{18}$ m. For comparison, the gravitational

radii of the black holes giving rise to the jets are $r_g = 1.5 \times 10^{12}$ m (M/10^9 M$_\odot$). The jets show a remarkable persistence in the face of many potentially destructive instabilities.

The potential of blazars to test our understanding of particle astrophysics (e.g. Dermer & Menon (2009); Dermer & Razzaque (2010)) and jet launching mechanisms provides a strong motivation for both observational and theoretical studies of these intriguing objects. However, in spite of intensive observational and theoretical investigations over the last five decades, the details of the structure and composition of blazar jets, and of the mechanisms through which jets are launched and collimated, accelerate non-thermal particle populations, and emit radiation, remain elusive.

Optical polarization observations probe the magnetic field structure and evolution in the relativistic jets, and thus provide the crucial coupling between the gamma-ray and radio emission in these systems. This work will result in a better understanding of the configuration and strength of the magnetic field in the gamma-ray emission zone. In combination with data from radio and gamma-ray wavebands it will enable competing jet composition, collimation, acceleration, and confinement theories to be tested.

4.3 Observational and Theoretical Challenges in the Study of Blazars

4.3.1 Observational Challenges

Beaming: Small variations in the angle between the jet axis and the line of sight induce large changes in the amount of relativistic beaming of blazar emission, and result in significant variations in all observable quantities that are affected by beaming and boosting (apparent luminosity, variability measures, apparent velocities of jet components, energy spectra). This effect in turn limits the repeatability of blazar behavior, and it induces large scatter in correlations between observables and physical properties of blazar jets.

Variability: Blazars are strongly variable on all timescales, and this property presents an additional observational complication in blazar studies. Because of nonregular variability, the properties of blazar populations cannot be straightforwardly determined through surveys alone, since these only capture a single snapshot of each source. Instead, blazars also need to be studied in the time domain. For this reason, systematic, concurrent multi-frequency and multi-technique observations of blazars are necessary rather than simply desirable.

Lack of spatial resolution: At most frequencies, blazar emission is spatially unresolved. As a result, and due to the close alignment between jet axis and line of sight, the received emission is an accumulation of photons from different locations along the jet. The location of the emission region in each frequency cannot therefore be directly determined through imaging; rather, it needs to be located by the combined analysis of a variety of observations (for example, by measuring time lags between flares at different frequencies) and by modelling.

4.3.2 Theoretical Challenges

From the theoretical perspective, although considerable progress has been achieved in the modelling of jet launching Blandford & Znajek (1977); Blandford & Payne (1982); Vlahakis & Tsinganos (1999); Vlahakis & Königl (2004); McKinney & Blandford (2009), particle acceleration, and non-thermal emission Dermer
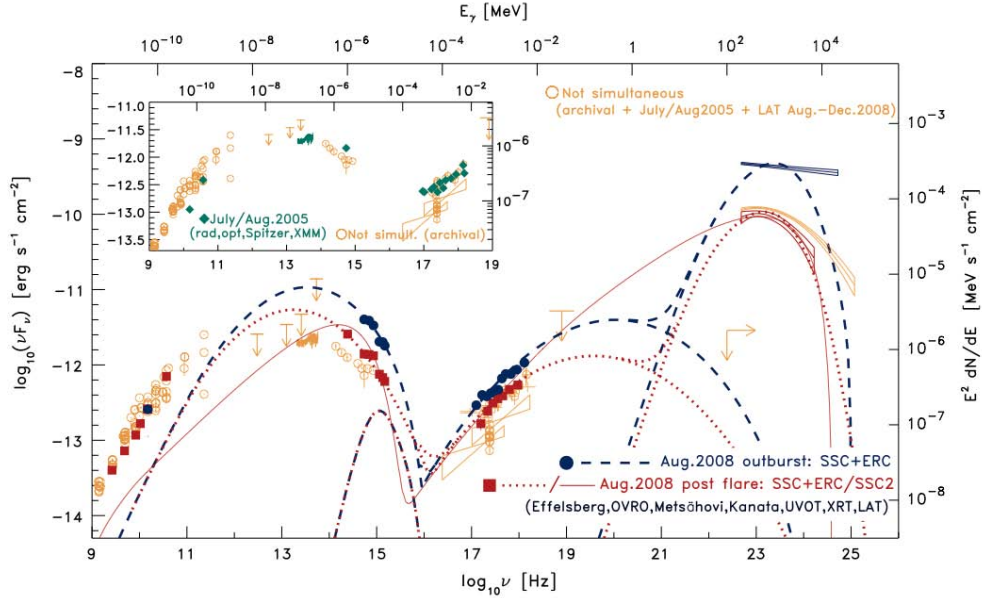
Figure 4.1: Broadband spectrum of blazar PKS 1502+106 (from Abdo et al. (2010c)), which extends over sixteen orders of magnitude in wavelength. Both the low- and high-frequency peaks are generated by non-thermal emission by relativistic particles (synchrotron and inverse Compton radiation, respectively). This source is a striking example of the degeneracies between different theoretical models (red solid and dotted lines, both of which can explain the post-flare data equally well.)

et al. (1992); Mannheim (1993); Sikora et al. (1994); Blandford & Levinson (1995); Krawczynski et al. (2002); Böttcher & Reimer (2004); Ghisellini et al. (2011); Nalewajko et al. (2011), degeneracies between the predictions of different models have slowed progress in model rejection and discrimination. For example, multiwavelength spectral modelling of blazars involves a large number of free parameters, and as a result physically different models can be tuned to fit the same datasets (see Figure 4.1). Characteristic examples include the composition of the jet and the primary emission mechanism in gamma-rays. Jets may be composed of an ion-electron plasma, accelerating both electrons and protons to very high energies, and the high energy emission could be due to proton interactions or proton-induced cascades (hadronic emission models). Alternatively, jets could be composed of an electron-positron plasma, in which case the accelerated particles are exclusively leptons, and the high-energy emission is due to inverse Compton scattering of soft photons to gamma-ray energies (leptonic emission models). Population models of blazars (luminosity functions, relation between spectra and luminosities, spectral index distributions) also suffer from considerable systematic uncertainties and have been long debated in the field. As a result, to this day there is no unique, accepted model or mechanism for: (i) the acceleration of the jets near the inner parts of the accretion disk; (ii) the composition of the jets; (iii) jet confinement; and (iv) particle acceleration and magnetic field production, and consequently non-thermal emission. Significant progress has been made on the modelling front recently; for instance, recent 3-D relativistic simulations (e.g. Broderick & McKinney (2010)) are able to produce robust observables – which highlight the importance of the magnetic field orientation and of rotation measures – that come through despite the high dependence on orientation. Tying together blazar flares over the whole electromagnetic range should enable us to identify robust signatures; we hope that the polarization angle rotation that is the focus of this proposal will prove to be one of these.
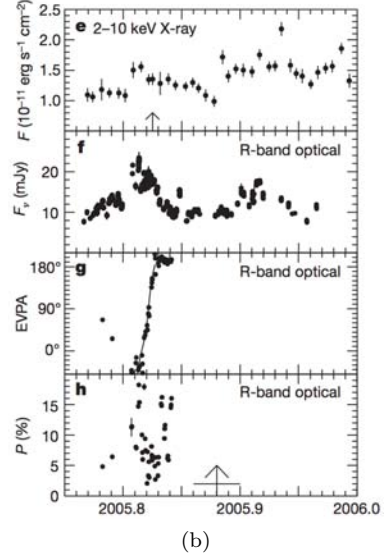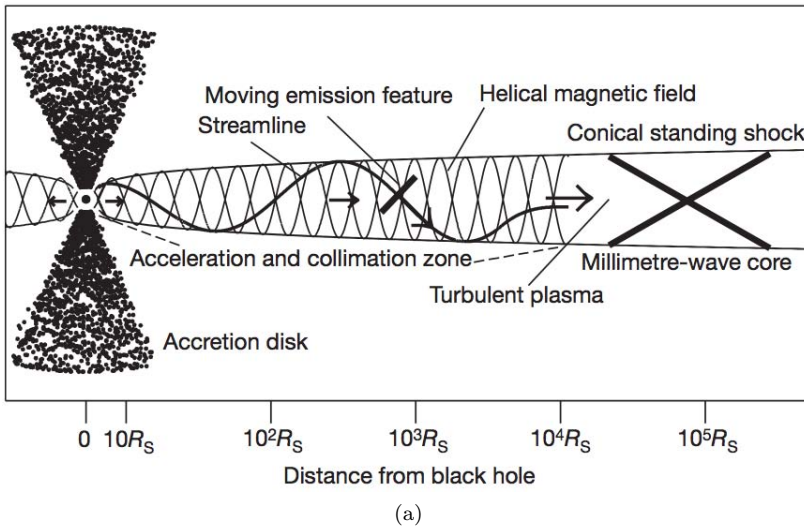
Figure 4.2: A model (a) and supporting data (b) of the inner jet of BL Lac from Marscher et al. (2008). An emission feature is accelerated along a streamline in the helical magnetic field. Its emission comes to dominate the emission from the rest of the jet as it enters the last spiral, and we see the optical polarization angle rotate before the emission feature exits the acceleration and collimation zone. We need to capture a significant number of these polarization flips in order to be able to do rigorous statistics on them and to be sure that selection effects are not biasing our conclusions.

4.4 Fast Optical-Polarization Changes During Gamma-ray Flares

A recent multi-wavelength campaign triggered by *Fermi* observations of blazar 3C279 and which included measurements of the blazar's optical brightness and polarization made a remarkable serendipitous discovery: the polarization angle of optical photons from 3C279 seemed to exhibit an almost 180-degree-angle rotation during a gamma-ray flare recorded by *Fermi* Abdo et al. (2010a) (see Figure 4.3). At the same time, the degree of polarization dropped from 30% to 10% during the flare, only to recover shortly after the source returned to pre-flare activity levels. However, there were only a few optical polarization data points during the transition. This paucity of data combined with the 180° ambiguity in polarization angles means that more data points during the gamma-ray flare (i.e. better sampling cadence) would be needed to conclude unambiguously that a smooth polarization rotation did indeed take place.

Similar polarization-rotation events have been observed in PKS 1510–089 Marscher et al. (2010), and in BL Lac Marscher et al. (2008) (however, the multiwavelength campaign that recorded the latter event occurred before the launch of *Fermi*, so GeV-energy data were not available and gamma-ray information came in TeV energies with the MAGIC telescope). These measurements are highly suggestive of a correlation between gamma-ray flares and the optical polarization angle, though this relationship needs confirmation with more statistics.

Polarized optical emission in blazars is produced by relativistic particles spiraling around magnetic field lines (the synchrotron component of the blazar spectrum). For this reason, polarization data probe the configuration and strength of the magnetic field in the emission region, critically narrowing the available model parameter space. As a result, this newly discovered class of events has prompted a series of theoretical modelling efforts aiming to explain the behavior of the degree and angle of the optical polarization during flares.
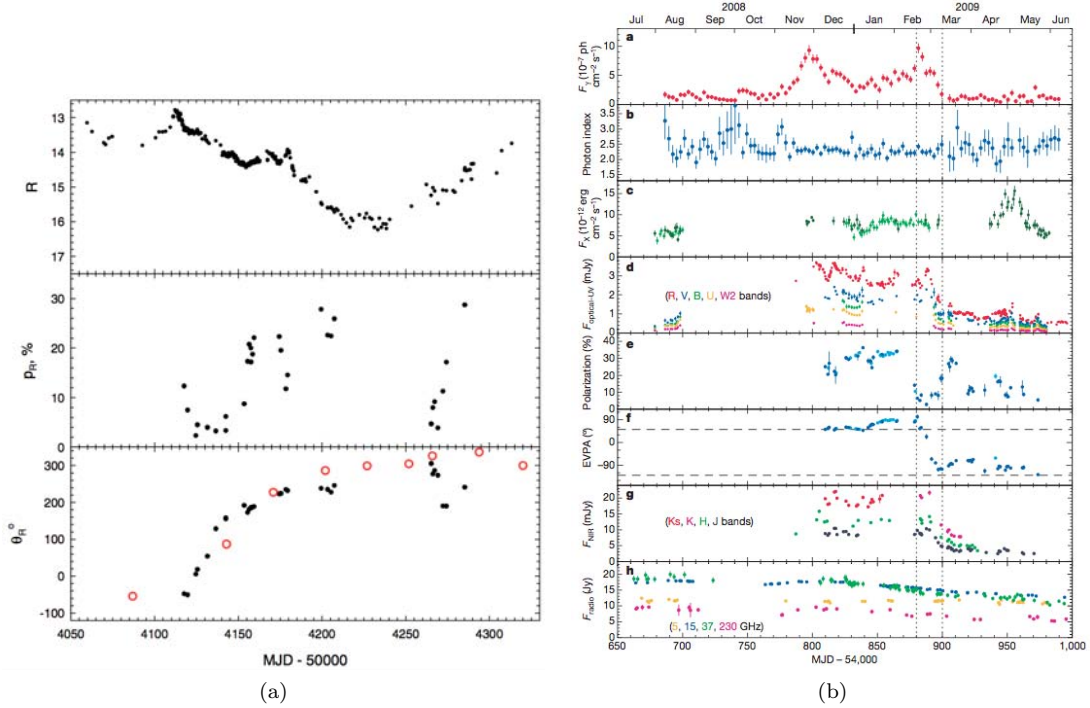
Figure 4.3: (a) The observed rotation in the optical polarization angle of 3C279 seen by Larionov et al. (2008) in 2006-2007. (b) Simultaneous multi-wavelength observations of 3C279 by Abdo et al. (2010a) in 2009. A flare in the gamma-ray photons **a** seems to be accompanied by a change in the polarization angle of the optical photons **f**, though the lack of optical polarization data points during the transition and the small number of such events detected encourages caution in assuming that they are physically related. This is a highly suggestive correlation which needs confirmation with more statistics. The polarization angle rotates in the opposite direction to that seen in (a), which is interpreted to favor a "bent jet" scenario over a helical path scenario.

Proposed interpretations for the flares in 3C279, PKS 1510–089 and BL Lac include magnetic field distributions that deviate from axisymmetry, a swing of the jet with respect to the line of sight, or the propagation of the emitting disturbance along a helical path in a magnetically dominated jet. Some of these scenarios are:

Helical path scenario: Two theories of jet collimation hold that the jet is gradually collimated either by a coiled toroidal magnetic field Vlahakis & Königl (2004) or external gas pressure Melia (2002). If magnetic forces gradually accelerate and focus the jet, the jet plasma will slow along streamlines that follow a helical trajectory with a wider pitch angle than that of the magnetic field Vlahakis (2006), as shown in Figure 4.2a. Using this model, Marscher et al. Marscher et al. (2008) interpreted a smooth rotation in the optical polarization angle of BL Lac over the course of 5 days (Figure 4.2b) as evidence of a knot of emission moving along a streamline in the acceleration and collimation zone. A similar event in PKS 1510–089 Marscher et al. (2010) unfolded over the course of 50 days. In this model, the high energy X- and gamma-ray emission seen during blazar flares is caused by shocks propagating through the acceleration and collimation zone. This region is opaque to radio waves due to synchrotron self-absorption; a radio flare would be expected to follow later when the emission feature enters a radio transparent part of the jet.
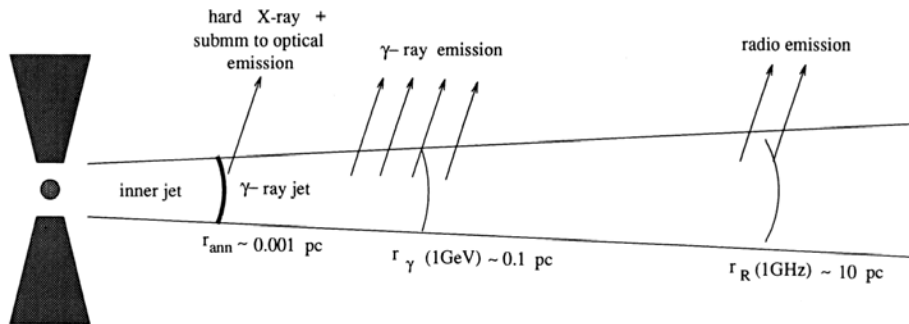
20

Figure 4.4: A cartoon depiction of the pair cascade model for gamma-ray emission from blazar jets, from Levinson (1996). Ambient soft X-rays are inverse-Compton scattered to gamma-ray energies by pair cascades in a relativistic jet. Synchrotron cooling of the pair cascades results in sub-mm to optical emission within the gamma-sphere, while radio emission occurs at greater radii where the jet is optically thin.

Bent jet scenario: An alternative theory to the helical scenario, invoked to explain the behavior observed in 3C279 Abdo et al. (2010a) (see Figure 4.3), is the "bent jet" scenario. The optical polarization angle of 3C279 was observed to rotate by 180° over the course of 20 days, coincident with a substantial gamma-ray flare. In the "bent jet" scenario, the blazar jet is curved and is oriented in such a way that the jet trajectory projected on the sky turns by almost 180°. The optical polarization behavior during a flare is explained by assuming that we observe a density pattern co-moving along the jet as it propagates through the bend: it swings around and appears to change direction, resulting in a smooth change in the observed optical polarization angle of 180°.

Pair-cascade scenario: The pair-cascade scenario Blandford & Levinson (1995); Levinson & Blandford (1995); Levinson (1996) holds that the gamma-ray emission in blazars occurs much closer to the central engine than the scenarios described above. A cartoon depiction of the model is shown in Figure 4.4. The gamma-ray emission results from the inverse Compton scattering of ambient soft X-rays from the hot accretion disk by relativistic pairs accelerated in situ by shock fronts in a relativistic jet. In this model the sub-mm to optical emission is produced by synchrotron cooling of cascading pairs *inside* the gamma-sphere. The radio (~ 1 GHz) photons are emitted from larger radii where the jet becomes optically thin. The implications of this model for the polarization properties of the optical emission are not well-explored: it is thought that they could be due to precessional-like motion of a jet at small radius with individual jet elements moving more or less ballistically Blandford et al. (2011).

However, further progress is hindered by the lack of information regarding the frequency and repeatability of such events. We do not know whether these events represent typical behavior in all blazars, typical behavior in some blazars, or are extraordinary events associated with only a special type of flare even within a single source. This problem can be overcome only with a systematic search for similar events in a large number of blazars; a statistical assessment of the fraction of gamma-ray flares that are associated with such changes in polarization fraction and angle, and vice versa; and high-cadence monitoring of the manner in which they unfold across the electromagnetic spectrum.

Fortunately, the continuous sky-scanning of the entire gamma-ray sky by *Fermi*, and the multi-frequency monitoring of a large sample of blazars in radio by the OVRO, MOJAVE, and F-GAMMA programs provide multiwavelength coverage of blazar flares at the very-high and very-low energy ends of their spectrum. The missing link is being able to identify and time-resolve such events with optical polarimetric observations.

21

The program we propose here aims to provide this missing link, by obtaining optical linear polarization monitoring of unprecedented scale and cadence. In this way, we will make available a unique and critical piece in the puzzle of blazar astrophysics, and we will help reject or refine physical models of the structure and evolution of blazar jets. This will be a step of fundamental importance in understanding the blazar emission process, which will allow us to explain some of the most energetic objects in the universe: how they come to be so energetic, how they relate with the cosmic evolution of supermassive black holes, and how their emission affects the formation and evolution of other galaxies in the universe.

4.5 RoboPol: A Systematic Study of Fast Optical-Polarization Changes in Blazar Jets

In spite of the obvious importance of rapid polarization events such as the one observed during the flare of 3C279 in constraining theoretical blazar models, the rate at which new events of this type are likely to be discovered with existing programs monitoring the optical polarization of blazars is expected to be (and has been) low: current programs follow small numbers of sources, and they are aimed at monitoring the way optical polarization varies over long timescales, rather than at the fast-changing events discussed above. This is because these fast optical polarization changes in supermassive black-hole jets simultaneous with gamma-ray flares are a recent discovery, and, as a result, the astronomical community was not set up to study it in a systematic way before the launch of *Fermi*.

To remedy this, we have established an international collaboration between the California Institute of Technology, the University of Crete in Greece, the Max-Planck Institute for Radioastronomy in Bonn, Germany, Nicolaus Copernicus University in Poland, and the Inter-University Centre for Astronomy and Astrophysics (IUCAA) in India. We have agreed to begin a new blazar monitoring campaign called RoboPol, specifically aimed at measuring and characterizing the optical polarization behavior of blazars during flares.

4.5.1 Ideal site and telescope

We will operate this program at the Skinakas Observatory[1], operated by the Astrophysics Group at the University of Crete and the Foundation for Research and Technology – Hellas (hereafter the Astrophysics Group in Crete, AGC). The Observatory at Skinakas is located on a 1750 m peak 50 km west of the city of Heraklion on the island of Crete and has been operated since 1986 by the AGC. Its location achieves the best atmospheric conditions for astronomical observations in Europe, comparable to several of the best facilities in the world, with median seeing of 0.7 arcsec Boumis et al. (2001).

The 1.3 m Ritchey-Chretien telescope at the Skinakas Observatory is a highly suitable facility for studying bright and highly variable sources such as blazars. Although relatively small in diameter, it has sensitive detectors more than capable of providing accurate light curves of blazars over long periods Papadakis et al. (2004) due to the excellent weather conditions on the island of Crete for most of the year. It is a well-equipped modern telescope, and it can be remotely/robotically operated. Crucially, we will have an unprecedented amount of telescope time for a monitoring program: an average of 4 nights a week for the entire duration of the observing season (8 months from March to November).

---

[1]http://www.skinakas.org.gr

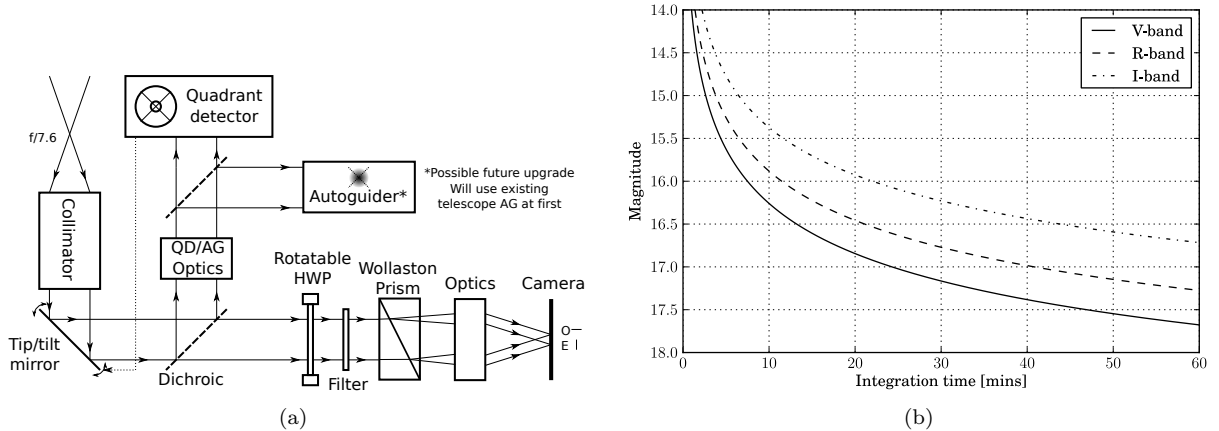(a)   (b)

Figure 4.5: (a) Design of specialized high-throughput polarimeter for the Skinakas 1.3 m telescope, currently under construction. A rotatable halfwave plate and Wollaston prism are used to separate photons with orthogonal linear polarizations. Two halfwave plate positions are needed for a measurement of the linear polarization vector. The tip-tilt mirror is a planned future upgrade to the instrument, funding permitting, though it is not essential for our program. (b) The integration time required to reach a SNR of 10:1 in the polarization angle measurement for a 2% polarized source; using the instrument shown in (a) installed on the Skinakas 1.3 m telescope and assuming 1" seeing.

4.5.2 A specialized instrument and an aggressive observing program

To be useful in resolving the open questions in blazar astrophysics, our campaign will meet three criteria:

1. **Observe a large number of blazars.** This will allow us to draw conclusions about how common polarization rotation during gamma-ray flares is, in a statistically significant way.

2. **Observe them often.** gamma-ray flares are rare; we need regular, high-cadence observations of the optical emission to catch potential short-duration events and ensure simultaneity with the *Fermi* data.

3. **Observe them dynamically.** If we observe a change in the optical polarization angle of a blazar, we will automatically change our observing schedule to confirm the measurement and concentrate on the varying blazar. In this way, we will ensure that the event is adequately resolved in time and followed until its conclusion.

Specialized instrument

The optical polarization observations will be conducted using a high-throughput optical polarimeter ($\sim 34\%$ efficiency for telescope and instrument), specially designed and built for the Skinakas 1.3 m telescope (see Figure 4.5a). The design and construction of the instrument has been privately funded. It is being built by a world-expert in optical polarimeters, Prof. A.N. Ramaprakash at IUCAA, who has built and successfully operated polarimeters in the field Ramaprakash et al. (1998). The polarimeter was designed with high observing efficiency and automated operation as prime goals. We expect to commission the polarimeter in the Northern summer of 2012, and begin regular observations shortly thereafter.

The RoboPol polarimeter uses a rotatable halfwave plate and a Wollaston prism to separate photons with orthogonal linear polarizations which are imaged by a CCD. Each object in the sky forms two images on the CCD; the linear polarization state is calculated from the number of photons in each image for two different halfwave plate positions (rotated by 22.5°). The field of view is designed to be 5'; this will allow us to obtain

relative photometry of the blazar using nearby standard catalog stars. The instrumental polarization will be measured by observing unpolarized stars in the field, as well as periodic measurements of unpolarized standard stars.

We will optimize our observing efficiency by only observing each source long enough to obtain a signal-to-noise ratio (SNR) of 10:1 in the linear polarization angle (EVPA). In Figure 4.5b we show the integration time needed to measure the EVPA with a SNR of 10:1 in three different bands. This is for a 2% polarized source, and we assume 1" seeing.

Observing sample

Our sample will be a predefined selection of bright and highly polarized gamma-ray blazars. The *Fermi* 1FGL sample of gamma-ray bright blazars Abdo et al. (2010b) contains 374 blazars that can be observed at an airmass less than 1.5 from the Skinakas Observatory ($-6.5° < \delta < 77°$). Of these, 139 are brighter than 17th magnitude in the R band as measured by the USNO-B catalog Monet et al. (2003).

While the optical polarization properties of the complete *Fermi* sample are not known, we can estimate the optical polarization distribution of the population (Figure 4.6a) using data from the University of Arizona observing program[2]. From this we estimate that around 115 blazars observable from Skinakas will be both brighter than 17th magnitude in the R band and more than 2% polarized. This potential sample size is more than a factor of 2 larger than any existing optical monitoring program currently operating, and about 10% of the total number of blazars detected by *Fermi*. The number of potential targets is increasing all the time as *Fermi* continuously detects more blazars (since blazars can persist in a low state for several years).

Observing strategy

AGC has committed to provide large amounts of observing time for this program: on average 4 nights a week at the 1.3 m telescope throughout the observing season – 8 months between April and November, when the site is accessible. This is a large amount of time by all astronomical standards, and it will allow us to meet our second criterion of frequent observations.

To satisfy the third criterion, a dynamic observing schedule, we will implement a "robotic" survey: the observing schedule will be handled dynamically by a smart control system capable of reducing the data in real time and making decisions on how to proceed with the observing. By automating the observing decisions we increase our efficiency, thereby making it feasible to observe a larger number of objects each night.

We estimate what cadence we might achieve by simulating a simple observing strategy: we generate an observing sample by assigning a polarization fraction drawn from the distribution in Figure 4.6a to all *Fermi* 1FGL blazars brighter than 17th magnitude in the R band. Each blazar is observed as it transits the meridian, and we observe with a two weeks on/two weeks off time allocation. We observe each blazar long enough to obtain a SNR of at least 10:1 in the linear polarization angle.

With this observing strategy we will be able to monitor the ~ 30 sources visible each night using only half the observing time available: the remainder of the night can be spent concentrating on sources undergoing rapid polarization events. We conclude that we will be able to achieve both monitoring of quiescent sources *and* higher-cadence observations of flaring events for a large ($\gtrsim 100$) sample of blazars. We show a typical annual coverage diagram in Figure 4.6b: the observed sources are sorted by right ascension along the ordinate. Observations are indicated by a black dot.

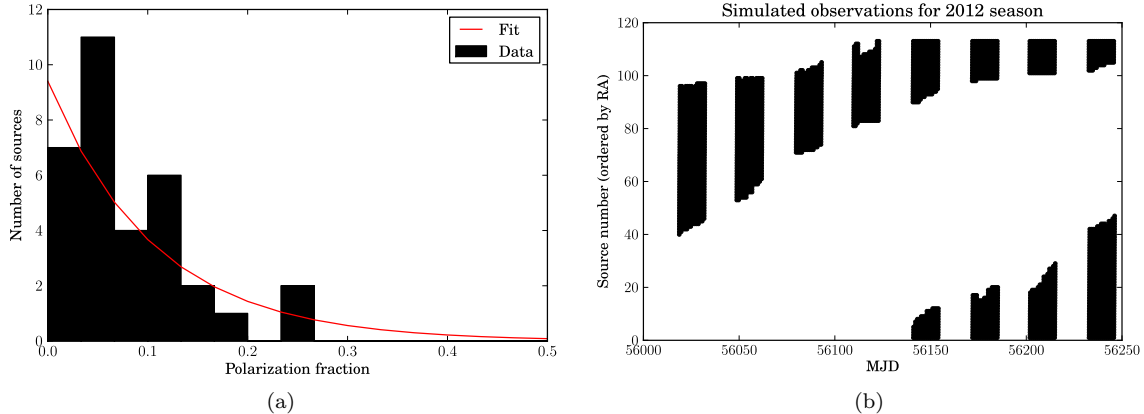[2]http://james.as.arizona.edu/~psmith/Fermi/

Figure 4.6: (a) The distribution of mean optical polarization fraction of *Fermi* blazars observed by Smith et al. (2009). The red line is the best-fit exponential function to the data. (b) The observation coverage obtained using the simple scheduling procedure outlined in the text.

With this simple strategy we should obtain about 4500 observations (counting only 1 observation per source per night) spread over 115 sources in 8 months of observing. For reference, the largest optical polarization program currently in operation obtained 1277 observations of 33 sources over the course of 1 year Smith et al. (2009). This is an estimate of the quiescent monitoring cadence we will achieve. There will be additional observations where we concentrate on sources undergoing rapid polarization events. Since the duration and frequency of these rapid events are not known – indeed the systematic study of this is part of the motivation for this project – it is not possible to estimate what sort of polarization rotation event coverage we will obtain.

4.5.3 Coordinated Multi-wavelength Coverage

We will mount a complementary monitoring campaign of the radio polarization of our blazar sample using the OVRO 40 m telescope, which is being upgraded with a new instrument to measure the linear polarization at 15 GHz (in addition to flux density). Furthermore, we will use the CARMA mm-array to follow up gamma-ray flares with linear polarization measurements at a wavelength of 3 mm. External collaborators at the Max-Planck Institute for Radioastronomy and the Nicolaus Copernicus University will provide additional radio- and mm-wavelength coverage of the blazar sample. The combination of *Fermi* gamma-ray data with contemporaneous linear polarization and flux density measurements at optical, mm and radio wavelengths will help illuminate the connections between the high-energy inverse compton peak and the low-energy synchrotron peak in blazar jet emission.

4.5.4 Theory and Phenomenology

In conjunction with our monitoring program, we will mount a concerted scientific analysis and interpretation campaign to interpret the data and extract full scientific value from it. Our interpretation campaign will follow two parallel axes:

- Physical modelling of the blazar emission region: We will develop physical models of increasing complexity, as data demand it, to model the region of the jet responsible for the flares associated with the rotation of the optical polarization angle. We will start with basic jet models connecting the energetics

of the emission, the time profile of the flares, and the evolution of optical polarization, with the black hole mass, accretion rate timescales, magnetic field geometry, and light-crossing times at the scale of the emission region, modulated by relativistic effects due to varying jet Lorentz factors. We will then increase the complexity of the model, including a more detailed treatment of the magnetic field, the acceleration and emission processes, and the time-dependent behavior of the propagation of shocks and disturbances along the jet. We will graduate to detailed MHD simulations of the evolution of the emission region, and sophisticated multi-component calculations of jet spectra.

- <u>Population studies and phenomenology</u>: Owing to the large size and strictly-defined selection criteria of our sample, and the long-term monitoring we plan to conduct, we will be able to build statistics on the incidence of fast polarization-rotation events in the population of blazars. In this way, we will be able to also study this phenomenon from the population-modelling perspective, and identify correlations between the incidence rate and properties (time profiles, duration, flare strength) of these events and other physical properties of the blazar jets where they occur (such as Lorentz factors, intrinsic luminosities, spectral properties, black hole masses, and environment). We will do so by explicitly simulating, with Monte-Carlo techniques, the effect of varying orientations and selection effects relevant for each dataset we use, as well as observational uncertainties, and systematic uncertainties entering through derived quantities (such as black-hole masses).

Chapter 5

KuPol: An instrument to monitor the radio linear polarization of blazars

5.1 Introduction

The 40 m telescope at OVRO, Figure 5.1, has been used to monitor the flux density of a very large sample of blazars since 2008. Over 1600 sources, 1200 of which are blazars, are monitored approximately twice-weekly. The goal of this effort is to assemble long time-series data of the radio behavior of a statistically complete sample of blazars.

Blazar emission is thought to be powered by relativistic jets closely aligned to the line of sight. They emit across the electromagnetic spectrum (see Figure 4.1) and are characterized by highly variable emission – particularly at gamma-ray wavelengths. Blazars have a characteristic double-humped spectrum. The longer-wavelength hump (from radio to optical) is powered by synchrotron radiation produced in the jet, while the short-wavelength hump (X-ray to gamma-ray and higher energy) is thought to be powered by inverse-Compton scattering of seed photons by the same ions which produce the synchrotron emission.

This is as far as consensus goes: the unanswered questions range from what the seed photons are to where in the jet the gamma-ray photons are produced. The effort at Caltech using the 40 m telescope is aimed at answering some of these questions. We aim to establish the relationship between gamma-ray photons – measured at low-resolution by the *Fermi* gamma-ray space telescope – and the radio emission, monitored at a broad range of resolutions from a variety of ground-based telescopes.

Synchrotron emission is intrinsically highly linearly polarized, as are blazars. This indicates a highly-ordered magnetic field in the blazar relativistic blazar jet at the source of the emission. By complementing the flux density information we currently gather with polarization information, we will be able to better-study the structure of the magnetic field which governs the acceleration and collimation, and hence the emission, of the jet.

To this end, I have designed and built a new receiver for the 40 m telescope called KuPol (the Ku-band Polarimeter). This receiver was designed to meet a broad range of requirements:

- Achieve a system temperature of 20 K in the total intensity channel. This is half as much as the existing receiver.

- Measure the total intensity in a beam-differenced fashion to remove the effect of atmospheric fluctua-

Figure 5.1: The OVRO 40 m telescope. It is a prime-focus telescope dedicated to monitoring the flux density of a large sample of blazars and other radio sources at 15 GHz.

tions.

- Add the ability to measure the linear polarization of each beam.

- Double the bandwidth of the system to 6 GHz.

- Perform the measurement in a large number of narrow channels to allow the rejection of radio-frequency interference (RFI).

The sum of all these requirements led to a novel receiver design which meets the requirements and is highly flexible, allowing it to meet a variety of future uses including transient detection, pulsar timing, and spectroscopic studies.

5.2   Receiver Design

The need to reject RFI from stationary and steady transmission beacons required a spectral digital backend design. I chose a continuous comparison radiometer architecture over a Dicke-switched architecture (as the current receiver is) for the beam differenced total intensity measurement, and a correlation polarimeter architecture for the linear polarization measurement.

The basic receiver design is shown in Figure 5.2. The cryogenic front-end section of the receiver and some RF electronics are housed at the prime focus of the 40 m antenna, as shown in Figure 5.3. The
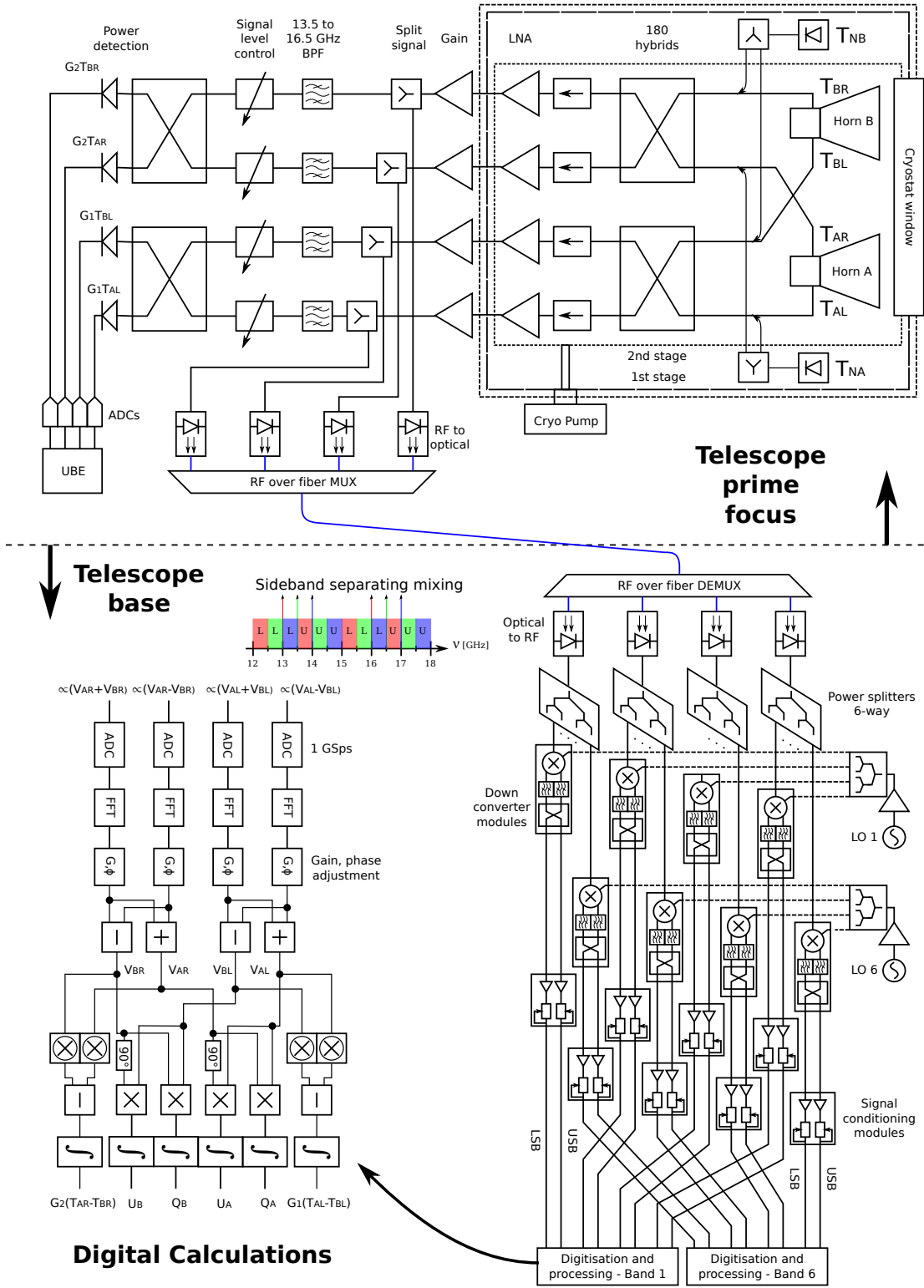
Figure 5.2: Simplified schematic of the KuPol receiver. A cryogenically-cooled front end is housed at the prime focus of the 40 m antenna (Figure 5.1). The signals which exit the cryostat are split: one half is processed with analog hardware while the other half is transported to the base of the telescope on optical fiber. The signal downconversion, digitization and processing happens here.

29

Receiver RF
cold plate

Vacuum
window

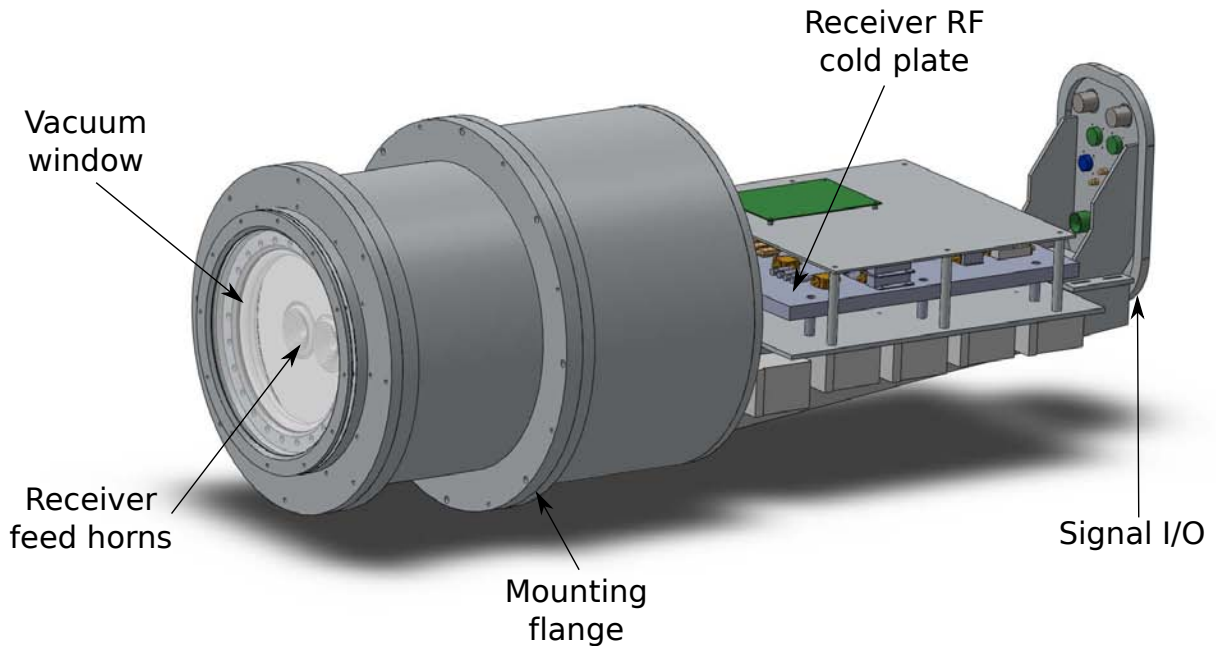Receiver
feed horns

Mounting
flange

Signal I/O

Figure 5.3: A CAD model of the receiver assembly mounted at the prime focus of the 40 m telescope. The rear section of the weather-proof can has been hidden to show the detail of the receiver RF cold plate. The receiver can houses the cryostat and additional RF electronics in a temperature-controlled environment. The full assembly is mounted to a focus ring at the prime focus of the telescope using a mounting flange, and can be easily removed for repair or upgrades.

cryostat contains two feed horns, with beams offset on the sky by 13 arcminutes, which each produce circular polarization signals. These are combined using 180° hybrids – designed in collaboration with Caltech graduate student Walter Max-Moerbeck – before being amplified by cryogenic low-noise amplifiers.

The signals exiting the cryostat, which are a combination of two circular polarization signals from each horn, are further amplified and split. One half of the split signals are processed with analog hardware to measure the beam-differenced total intensity of the signal as a sanity-check of the digital processing. The other half of the RF signals are transmitted by optical fiber (the intensity of a near-infrared laser is modulated by the RF signal in a process much like that used in AM radio) down the feed leg, through the elevation and azimuth wraps, and into the control room where the remaining RF and digital hardware is located. Here they are further amplified before being mixed to baseband and digitized. The processing necessary to measure beam-differenced total intensity and the linear polarization of each horn is performed using FPGA-based off-the-shelf ROACH boards from the CASPER group.

5.3 Cryostat Design

The KuPol cryostat's primary purpose is to cool the feed horns and the cryogenic low-noise amplifiers (made by Sandy Weinreb at Caltech) to about 10 K. Doing so greatly increases the sensitivity of the instrument. However, this requires a very large window on the cryostat, with a diameter of ~ 9". A 0.014" thick sheet of Mylar is used as a window material. The chamber in front of the cryostat window is covered by a sheet of radio-transparent foam. This fulfills two purposes: it protects the Mylar window from damage, and is filled
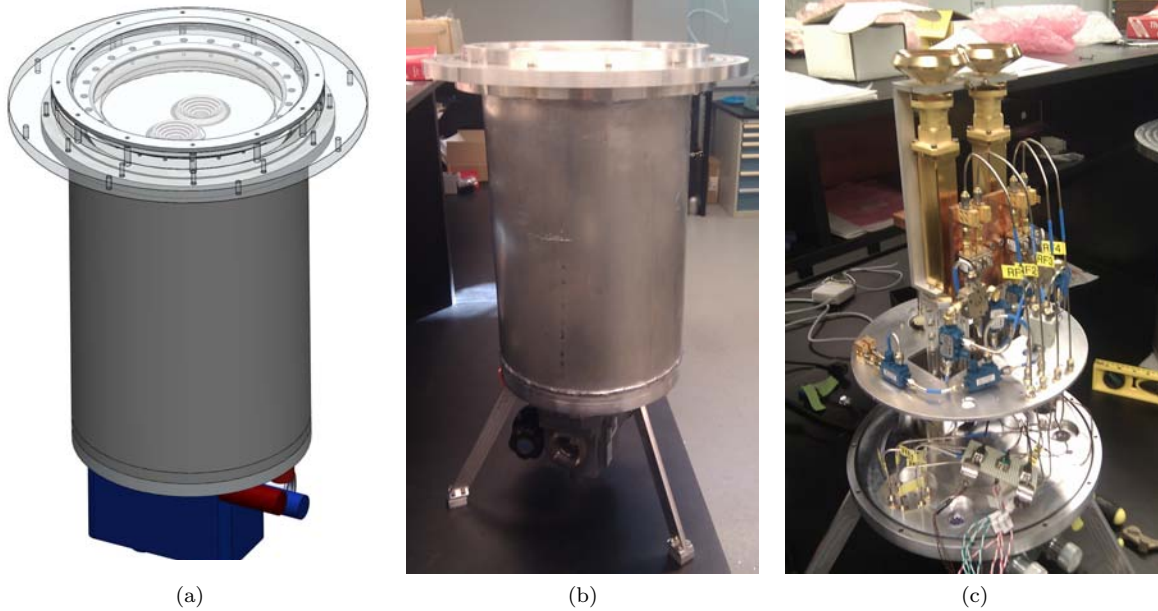
Figure 5.4: (a) 3D CAD model of the KuPol cryostat. The interior of the cryostat (feed horns and 40 K heat shield) can be seen through the window. (b) The fabricated cryostat in the lab. (c) The interior of the cryostat with the 10 K and 40 K RF components in place.

with nitrogen gas to keep water vapor from the cryostat window, thereby preventing condensation which would corrupt the data.

Cooling is provided in two stages by a CTI-350 cryocooler. Noise diodes which provide calibration signals are housed inside the cryostat on the first (40 K) stage. Provision is made for test signals to be injected into the cryostat when sealed in order to test the operation of the hardware and confirm proper operation.

The CAD model of the cryostat, a picture of the finished product, and a picture of the interior of the cryostat are shown in Figure 5.4.

5.4   Downconversion Hardware

Before the RF signals from the receiver front end (which cover the 12 to 18 GHz band) can be digitized, they must be converted to baseband and their level must be controlled. I split the 6 GHz wide RF band into 12 channels, each 500 MHz wide. These channels are mixed to 500 MHz to 1 GHz by a quadrature mixing scheme. This allows us to digitize at 1 Gsps and access the full 500 MHz bandwidth, while avoiding the poor ADC performance below 10 MHz.

The mixing scheme is shown graphically in Figure 5.2. Each down-converter and signal conditioning crate converts two 500 MHz bands to baseband – the upper sideband (USB) starting 500 MHz *above* the LO frequency, and the lower sideband (LSB) ending 500 MHz *below* the LO frequency. Six crates are needed to convert the full RF band to baseband. An important feature of the crate design is that the hardware for all the crates is identical, except for the LO source. This duplication of hardware allows us to take advantage of cost-breaks and economies of scale in assembly. A picture of the down-converter and signal conditioning crate, and the excellent image rejection achieved, is shown in Figure 5.5.

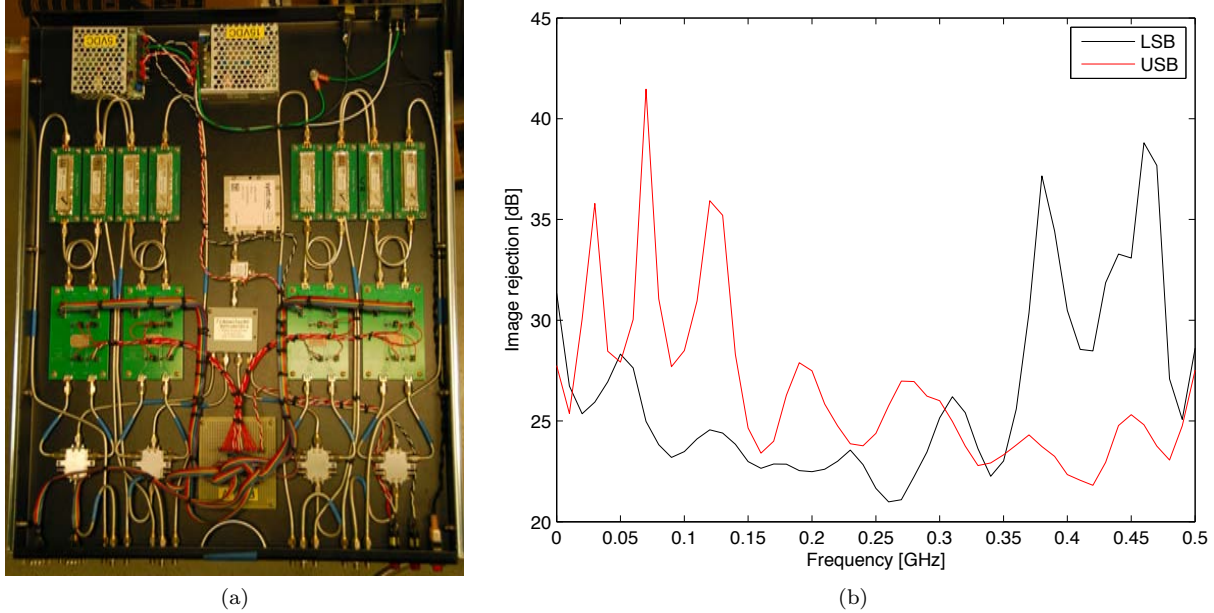(a)   (b)

Figure 5.5: (a) A KuPol down-converter and signal conditioning crate. It converts two 500 MHz wide bands (LSB and USB) to baseband (500 MHz to 1 GHz) for digitization and processing. (b) The measured image rejection of the quadrature mixing scheme.

5.5 Digital Backend Design

The digitization and processing of the baseband signals is performed by off-the-shelf hardware from the CASPER project[1]. We use the ROACH digital processing board, which is based on a Virtex-5 FPGA, and the iADC digitizers. The CASPER project provides both the hardware designs (fabricated by a private vendor) and a suite of MATLAB Simulink libraries. These libraries make it substantially easier to program the FPGAs.

One of the major advantages of using FPGA-based digital processing hardware is their reconfigurability. It takes only seconds to write a new processing code to the FPGA fabric, allowing the same hardware setup to act as many different types of instruments. One of the primary drivers for moving to a digital architecture is that it allows spectral information to easily be obtained. This allows us to identify and reject man-made radio-frequency interference.

The default configuration for the KuPol receiver is shown in Figure 5.2: it measures the beam-differenced total intensity and the linear polarization of each horn in 128 bins across each 500 MHz band. The FPGA software for this was developed by a Caltech undergraduate SURF student, Kirit Karkare, and Charles Copley, a DPhil student at Oxford.

The KuPol receiver is a powerful, flexible instrument that will allow the 40 m telescope at OVRO to perform cutting-edge astronomy now and well into the future.

---

[1]https://casper.berkeley.edu/wiki/Main_Page

Bibliography

Abdo, A. A., et al. 2010a, Nature, 463, 919

—. 2010b, The Astrophysical Journal Supplement, 188, 405

—. 2010c, The Astrophysical Journal, 710, 810

Blandford, R., McKinney, J. C., & Zakamska, N. 2011, Pramana, 77, 53

Blandford, R. D., & Konigl, A. 1979, Astrophysical Journal, 232, 34

Blandford, R. D., & Levinson, A. 1995, Astrophysical Journal, 441, 79

Blandford, R. D., & Payne, D. G. 1982, Monthly Notices of the Royal Astronomical Society, 199, 883

Blandford, R. D., & Znajek, R. L. 1977, Monthly Notices of the Royal Astronomical Society, 179, 433

Böttcher, M., & Reimer, A. 2004, The Astrophysical Journal, 609, 576

Boumis, P., Mavromatakis, F., Steiakaki, A., Paterakis, G., & Papamastorakis, J. 2001, Astronomische Gesellschaft Abstract Series, 18

Broderick, A. E., & McKinney, J. C. 2010, The Astrophysical Journal, 725, 750

Carretti, E., Tascone, R., Cortiglioni, S., Monari, J., & Orsini, M. 2001, New Astronomy, 6, 173

Caves, C. M. 1982, Physical Review D (Particles and Fields), 26, 1817

Chiang, H. C., et al. 2010, The Astrophysical Journal, 711, 1123

Cleary, K. A. 2010, Millimeter, 7741, 70

Collaboration, Q., et al. 2011, The Astrophysical Journal, 741, 111

Davis, R. J., et al. 2009, Journal of Instrumentation, 12, 12002

Dermer, C. D., & Menon, G. 2009, High Energy Radiation from Black Holes: Gamma Rays

Dermer, C. D., & Razzaque, S. 2010, The Astrophysical Journal, 724, 1366

Dermer, C. D., Schlickeiser, R., & Mastichiadis, A. 1992, Astronomy and Astrophysics, 256, L27

Ghisellini, G., et al. 2011, Monthly Notices of the Royal Astronomical Society, 411, 901

Hamaker, J. P., Bregman, J. D., & Sault, R. J. 1996, Astronomy and Astrophysics Supplement, 117, 137

Hu, W., Hedman, M. M., & Zaldarriaga, M. 2003, Physical Review D, 67, 43004

Jarosik, N., et al. 2003, The Astrophysical Journal Supplement Series, 145, 413

King, O., et al. 2012, ApJ (in prep.)

King, O. G. 2010, Twenty-First International Symposium on Space Terahertz Technology, 379

Krawczynski, H., Coppi, P. S., & Aharonian, F. 2002, Monthly Notice of the Royal Astronomical Society, 336, 721

Larionov, V. M., et al. 2008, Astronomy and Astrophysics, 492, 389

Larson, D., et al. 2011, The Astrophysical Journal Supplement, 192, 16

Levinson, A. 1996, Astrophysical Journal v.459, 459, 520

Levinson, A., & Blandford, R. 1995, Astrophysical Journal v.449, 449, 86

Mannheim, K. 1993, Astronomy and Astrophysics, 269, 67

Marscher, A. P., et al. 2008, Nature, 452, 966

—. 2010, The Astrophysical Journal Letters, 710, L126

McKinney, J. C., & Blandford, R. D. 2009, Monthly Notices of the Royal Astronomical Society: Letters, 394, L126

Melia, F. 2002, American Astronomical Society, 200, 951

Mennella, A., Bersanelli, M., Seiffert, M., Kettle, D., Roddis, N., Wilkinson, A., & Meinhold, P. 2003, Astronomy and Astrophysics, 410, 1089

Monet, D. G., et al. 2003, The Astronomical Journal, 125, 984

Nalewajko, K., Giannios, D., Begelman, M. C., Uzdensky, D. A., & Sikora, M. 2011, Monthly Notices of the Royal Astronomical Society, 413, 333

O'Dea, D., Challinor, A., & Johnson, B. R. 2007, Monthly Notices of the Royal Astronomical Society, 376, 1767

Papadakis, I. E., Samaritakis, V., Boumis, P., & Papamastorakis, J. 2004, Astronomy and Astrophysics, 426, 437

Pozar, D. 2005, Microwave Engineering, 3rd edn. (John Wiley & Sons Inc.)

QUIET Collaboration et al. 2011, The Astrophysical Journal, 741, 111

Ramaprakash, A. N., Gupta, R., Sen, A. K., & Tandon, S. N. 1998, Astronomy and Astrophysics Supplement, 128, 369

Sikora, M., Begelman, M. C., & Rees, M. J. 1994, Astrophysical Journal, 421, 153

Smith, P. S., Montiel, E., Rightley, S., Turner, J., Schmidt, G. D., & Jannuzi, B. T. 2009, eprint arXiv:0912.3621

Vlahakis, N. 2006, Blazar Variability Workshop II: Entering the GLAST Era ASP Conference Series, 350, 169

Vlahakis, N., & Königl, A. 2004, The Astrophysical Journal, 605, 656

Vlahakis, N., & Tsinganos, K. 1999, Monthly Notices of the Royal Astronomical Society, 307, 279

Wedge, S., & Rutledge, D. 1991, Microwave and Guided Wave Letters, IEEE Transactions On, 1, 117

Zmuidzinas, J. 1999, The Physics and Chemistry of the Interstellar Medium, 423

—. 2003, Applied Optics, 42, 4989